RECENT PROGRESS IN ENTRY RADIATION MEASUREMENTS IN THE NASA AMES ELECTRIC ARC SHOCK TUBE FACILTY

Brett A. Cruden[(1)]

[(1)]*ERC Inc at NASA Ames, MS 230-3, Moffett Field, CA 94035, E-mail:Brett.A.Cruden@nasa.gov*

ABSTRACT

The Electric Arc Shock Tube (EAST) at NASA Ames Research Center is NASA's only working shock tube capable of obtaining conditions representative of entry in a multitude of planetary atmospheres. The facility is capable of mapping spectroscopic signatures of a wide range of planetary entries from the Vacuum Ultraviolet through Mid-Wave Infrared (120-5500 nm). This paper summarizes the tests performed in EAST for Earth, Mars and Venus entries since 2008, then focuses on a specific test case for CO_2/N_2 mixtures. In particular, the paper will focus on providing information for the proper interpretation of the EAST data.

1. EXPERIMENTAL

The EAST facility consists of two shock tubes, both driven by an arc driver. The majority of work is performed on a 10.16 cm diameter Aluminum shock tube. The test section, located 7.5 m downstream of the diaphragm, consists of two 12 cm horizontal slot windows mounted opposite each other. Two sets of optics image through each window at different angles, so that four spectra are obtained with each shot. Each set of optics/spectrometer/detector is designed for different wavelength regions, covering Vacuum Ultraviolet (120-500 nm, "VUV"), UV/Visible (200-600 nm, "Blue"), Visible/Near Infrared (480-900 nm, "Red") and Infrared (800-5500 nm, "IR"). The second, which has been inactive until recently, is a 60 cm diameter, 21.5 m long stainless steel tube.

The driven section of the tube is filled with the planetary gas of interest – Air (79% N_2, 21% O_2) for Earth and CO_2/N_2 mixtures for Venus (96.5/3.5) and Mars (96/4). The tube is filled to a pressure to reproduce the gas density at the altitude of interest. Variation of the energy into the arc driver (generally 10-40 kV on a 861 μF capacitor bank) is used to tune the velocity. Often, conditions are chosen to reflect a particular entry trajectory, though in some cases the conditions are chosen for scientific purposes.

2. RESULTS

The typical format of data obtained in EAST is shown in Fig. 1 below. A 3D map of absolute spectral radiance is obtained as a function of position and wavelength. Cross-sections taken in the vertical direction may be used to obtain spatial (and corresponding temporal) radiance profiles for analysis of non-equilibrium excitation and relaxation. Horizontal cross-sections are averaged in the "equilibrium" region to predict and analyze equilibrium radiance characteristics.

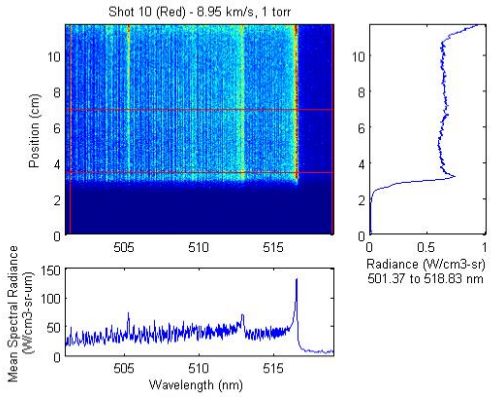

Fig. 1. Example of radiance measurement versus position and wavelength for a Venus entry condition.

Since 2008, eight test series have been conducted in EAST and are listed in Table 1 below. Data from each test series are archived and publically available. Access to the data can be provided by contacting the author.

Table 1. EAST Tests since 2008

Test Series	Year	Gas	Velocity Range (km/s)	Pressure Range (Torr)	Other Details
47	2009	Air	10	0.1-0.7	Checkout
48	2009-10	Mars	3-9	0.1-1.0	
49	2009	Venus	7-12	0.5-2.0	
50	2010	Air	8-12	0.1-1.0	
51	2011	Mars	6.5-7.5	0.05-0.25	
52	2011	Air	11-15	0.1-0.2	
53	2012	Mars	6.5-7.5	0.05-0.1	24" Tube
54	2012	Mars	3-8	0.1-1.0	Vary %N_2

Fig. 2 shows a graphical summary of the conditions investigated throughout these test series on a plot of laboratory pressure versus velocity. Also shown on the plots are the trajectories for various missions and mission studies. In these cases, the trajectories have been converted to their equivalent laboratory pressure via the ideal gas law so that the gas freestream densities are identical.

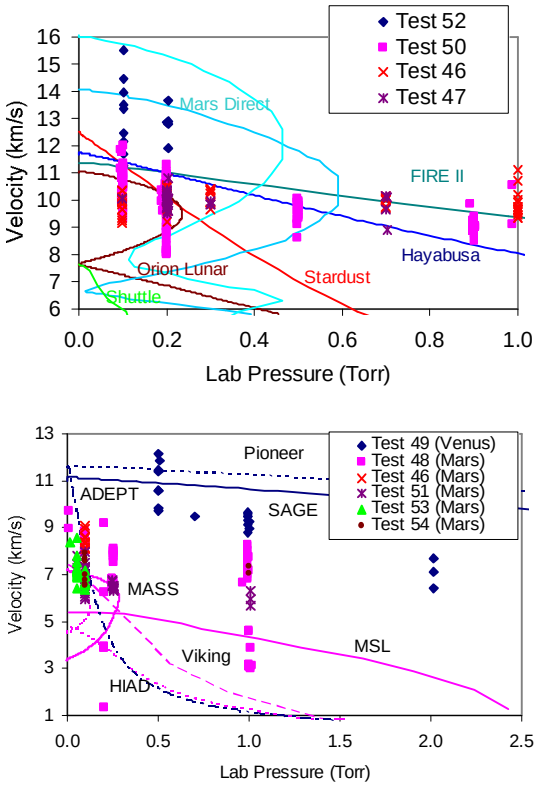

Fig. 2. Range of conditions studied in recent EAST tests in comparison to various mission trajectories. (top) Air entries, (bottom) Mars and Venus entries.

2.1. ESA Radiation Test Case

A working group of the ESA Radiation Workshop has organized a radiation test case (TC2-M5) in order to obtain a cross-facility comparison that could also be rebuilt theoretically. The test case called for tests in a Mars gas simulant (96/4 CO_2/N_2) at 7, 7.5 and 8 km/s and pressures of 0.1 Torr (13.3 Pa) and 1.0 Torr (133 Pa). These test cases are similar to some cases run in EAST during tests 48 (1 Torr) and 51 (0.1 Torr). Additionally, cases were run specifically for these purposes in Test 54. Because the velocity in EAST is not exactly repeatable, the shots were performed with the objective of spanning the general velocity range of 7-8 km/s, instead of exactly matching the velocity condition.

During Test 54, it was decided to perform 5 shots at each pressure conditions with fixed spectral coverages. In tests 48 and 51, the spectral coverages were more varied. The coverage is shown graphically in Fig. 3, with the color coding indicating the perceived quality of the data collected.

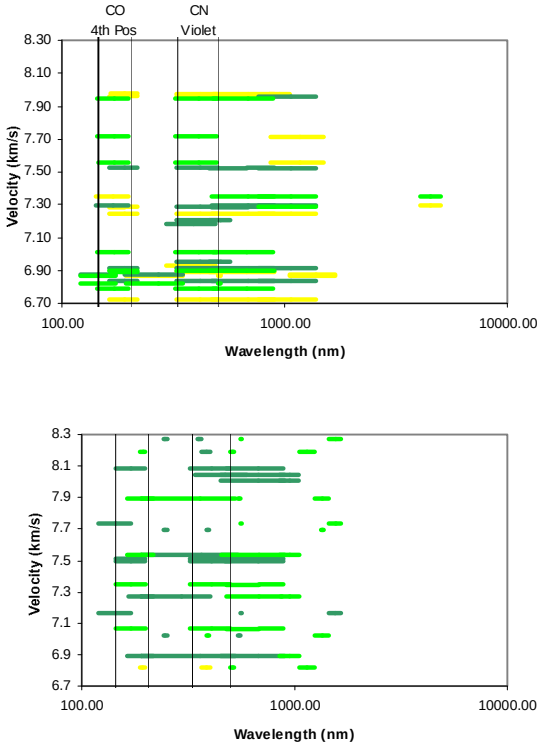

Fig. 3. Spectral ranges covered during EAST tests. (top) 0.1 Torr (13 Pa). (bottom) 1.0 Torr (133 Pa). The color indicates the approximate quality of the data (yellow - low, dark green - medium, bright green - high). Also shown are the approximate spectral regions for CO 4th Positive and CN Violet.

In the vaccuum ultraviolet, there were primarily three spectral ranges covered, including deep VUV (120-175 nm) and near VUV (165-220 nm) in Tests 48, 51 and an intermediate range (145-200 nm) in Test 51 and 54. These spectral ranges are determined by the window material installed during each test (LiF/MgF_2, silica or sapphire, respectively). For the 1 Torr condition, high resolution (188-198 nm, 242-254 nm) images were also collected of the C 193 and 248 nm lines. In the Vis/UV (Blue) range, the primary condition from 330-500 nm captures the major spectral features of CN Violet. Some spectra were also collected from 190-330 nm in Tests 48 and 51, however this region is largely dim and featureless. Additionally, Test 48 (1 Torr) includes some medium and high-resolution

imagery of the CN (0,0) and (1,0) band heads (365-405 nm, 386-397 nm and 351-363 nm). The Vis/NIR (Red) camera has primarily imaged from 480-900 nm where the C_2 Swan and CN Red is observed. A few shots included high resolution of the (0,0) and (0,1) C_2 Swan Bands from 501-519 nm, 540-560 nm, and 557-565 nm. In the Near IR, broad surveys of the extended CN Red band have been conducted from 760-1390 nm, 860-1490 and 1060-1690 nm. In Test 48, because of differing spectrometer resolutions, the ranges were split into approximately 850-1050 nm, 1050-1250 nm, 1250-1450 nm and 1450-1650 nm. One higher resolution spectrum was collected from 1330-1370 nm. Finally, two images of CO vibrational radiation from 4000-5000 nm were collected using a mid-IR camera.

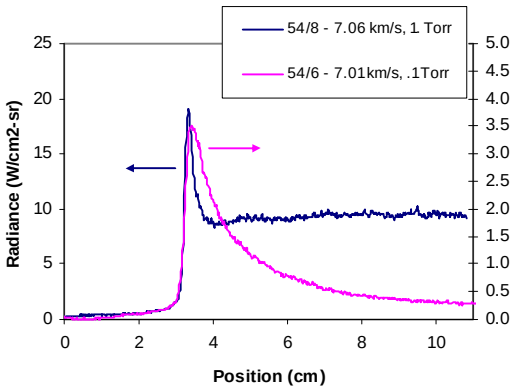

Fig. 4. Temporal decay characteristics of the CN Violet region of the spectrum (333-496 nm).

The characteristics of the shock at 0.1 Torr and 1.0 Torr are significantly different. Fig. 4 shows the temporal trace of radiance in the CN Violet regions for two shocks with a nominal speed of 7 km/s at the two pressures. In addition to being about 5 times as intense at its peak, the 1.0 Torr condition shows a fairly abrupt transition to a steady state value in about 6 mm. The 0.1 Torr case, on the other hand, shows a very slow relaxation. What is not apparent from this cross-section is that contamination from the driver gas is present at x=6.7 cm. Therefore, the region beyond this may not be valid for interpretation. However, in none of the 0.1 Torr tests is a steady state level of radiance observed within the duration of the test time. The data at 0.1 Torr therefore is only suitable for analysis of non-equilibrium radiation while the 1.0 Torr cases may be used for validating equilibrium predictions.

Radiance characteristics over the entire spectrum are shown in Fig. 5. On a log scale, spectra from the same pressure appear clustered together. The variation from 7-8 km/s may impart a factor of 2-3 change in radiance magnitude. This is illustrated in Fig. 6 which summarizes the radiance magnitudes as a function of velocity utilizing data from multiple EAST tests over the range of 5-10 km/s. Data at 1 Torr represents the nominal equilibrium radiance level, while the 0.1 Torr data has been integrated from ±2 cm from the peak of non-equilibrium volumetric radiance, assuming the gas to be optically thin. The data shown is particular to the CN radiance region of 333-496, but qualitatively similar data are obtained in other parts of the spectrum as well.

2.2 Interpreting EAST Data

2.2.1 Data contents

The EAST data is publically available from the EAST Data Repository through the NASA Safety Center Knowledge Now (https://nsckn.nasa.gov) site. Users should register on-line and then contact the author for access to the data repository. General information about the tests and conditions may be found in the on-line wiki, while the actual data files are found in the Document Explorer section. The tests are posted as

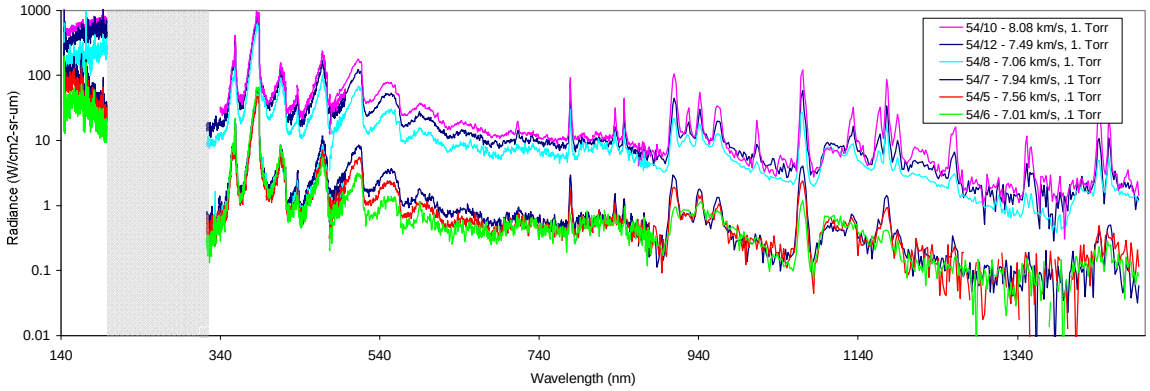

Fig. 5. Composite spectra for the six nominal test cases

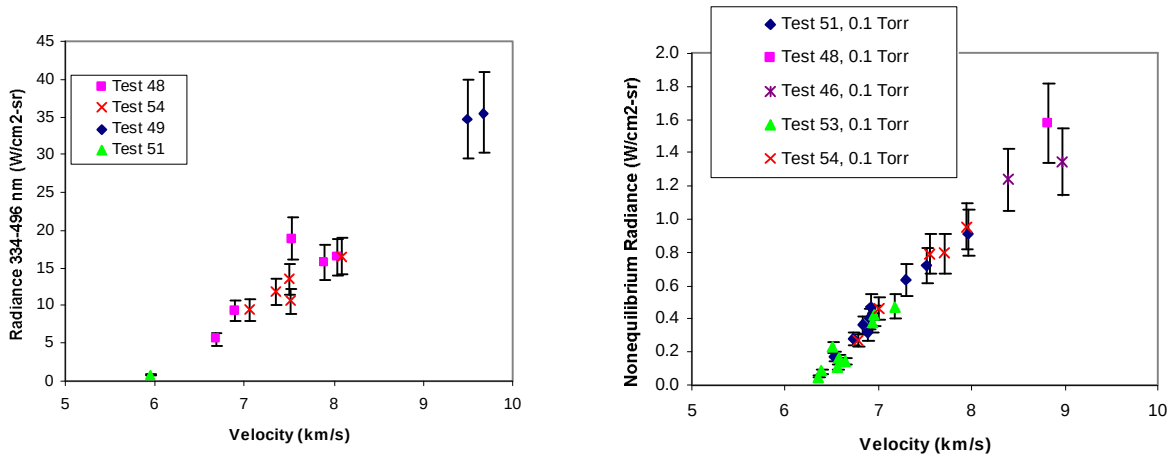

Fig. 6. Summary of integrated radiances from different EAST data sets from 333-496 nm. (top) Equilibrium radiance at 1.0 Torr. (bottom) Nonequilibrium radiance at 0.1 Torr, with optically thin assumptions.

.rar archive files in the general section or as individual files within the directory structure. The directory structure of a data release contains the following:

README.txt - Summary of the test and data contents
Shot Summary.xls - Key data for all shots in the test series
Data Sheets - Individual Data Sheets for each shot
Calibrated Data - 3D data files
Cross-Sections - Selected 2D cross-sections
Lineshapes.xls - List of instrument lineshapes

For each test series, the summary of all shots is given in the file Shot Summary.xls. This file contains, for each shot, key information including pressure, velocity and the spectral range covered by the instrumentation. Each spectral range is color coded to indicate the quality of the data. Red indicates no data was obtained and orange indicates data of unusable quality. The best quality data is highlighted in bright green, while the darker green suggests the data may be in disagreement with the rest of the data set. Yellow indicates useable data with either significant deviation from the rest of the data or some other identified problem, which would typically be noted under the comments field. It should be noted that, except for the red and orange, these ratings are subjective and should not necessarily be used to exclude or champion certain data over others.

For each individual shot, a data sheet containing the experimental parameters of the shot is contained within the Data Sheets folders. While most of the information within these sheets would not be necessary to interpret the data, a few key parameters are needed to construct a synthetic spectra that may be compared to the EAST data. This includes the spectrometer slit settings and camera exposure times. The impact and treatment of these two items are discussed in the following section. The impact of the slit parameters is summarized within the Instrument Lineshapes worksheet for each test series.

The calibrated data files are presently provided in one of two formats. The .SPE format is the format native to the PI-Acton software WinSpec, which is used to collect the spectra. The spectra in the .SPE format have been converted to absolute radiance units of $\mu W/cm^2$-sr-μm. These units are convertible to the more useable W/cm^2-sr-nm by dividing by 10^3 or to an equivalent volumetric radiance (W/cm^3-sr-nm) by dividing by 10^4 (for a 10cm diameter tube). X and Y calibration factors are stored as second and first order polynomial coefficients, respectively, within the header file. Routines are provided on the nsckn website for importing the SPE format into Matlab or IGOR. Details of the file format are publicly available and may be shared if requested. Users are encouraged to share additional conversion routines. The second format available is as Matlab .fig files, which appear similar to Fig. 1 above. Data may be extracted directly from the xdata, ydata and cdata fields of the surface plot with the Matlab get command. In general, the Matlab fig files are presented in volumetric spectral radiance for tests 47-53 and spectral radiance starting on Test 54. Finally, upon request, ASCII versions of the files will be provided, although this corresponds to a significant increase in file size.

The spectral cross-sections folder contains one excel workbook for each good shot. Each workbook contains 4 worksheets, one for each spectrometer. The worksheets include a spectral cross-section and (in

some cases) spatial cross-sections. Generally, the spectral cross-section is an average radiance collected somewhere behind the shock front in a nominal equilibrium region. However, in many cases (particularly at 0.1 Torr), no equilibrium exists in the valid test time. The temporal cross-sections are integrated over spectral ranges specified on the worksheet.

2.2.2 Data interpretation

The data is presented in the form of a radiance map as a function of position and wavelength. Proper interpretation of the data requires some additional knowledge of the experimental artifacts. This includes test duration, instrument lineshape, and spatial/ temporal smearing. These will each be discussed in turn.

2.2.2.1 Test Duration

The data presented is a snapshot of a moving shockwave. Basic shock tube theory explains that a shock wave generated within a shock tube consists of a primary (incident) shock front where the test gas transitions from its cool, low density freestream state to the shock-heated gas. This is followed by a contact front, where the composition changes from that of the heated shocked gas to the expanded driver gas. This transition has no pressure discontinuity but will have a discontinuity in temperature and density. The valid test gas under study consists of that bounded by these two fronts. While some ideal formulas exist for calculating the separation between the shock and contact fronts, the actual separation is typically much smaller due to the non-idealities of diaphragm breakage and arc heating. This front is often observed in the spectral image and it is important that it be correctly identified for the data interpretation to be meaningful.

Fig. 7 shows four images collected in one shot. The horizontal lines mark the approximate location of shock fronts and contact fronts. The shock front is observed in different locations on different cameras. This is because each camera has a different delay relative to the trigger signal. Also, for this reason the *exact* location of the shock front is not precisely known. The only thing that can be unambiguously assigned from the data is the onset of shock radiation.

Typically, the contact front is most readily observed in

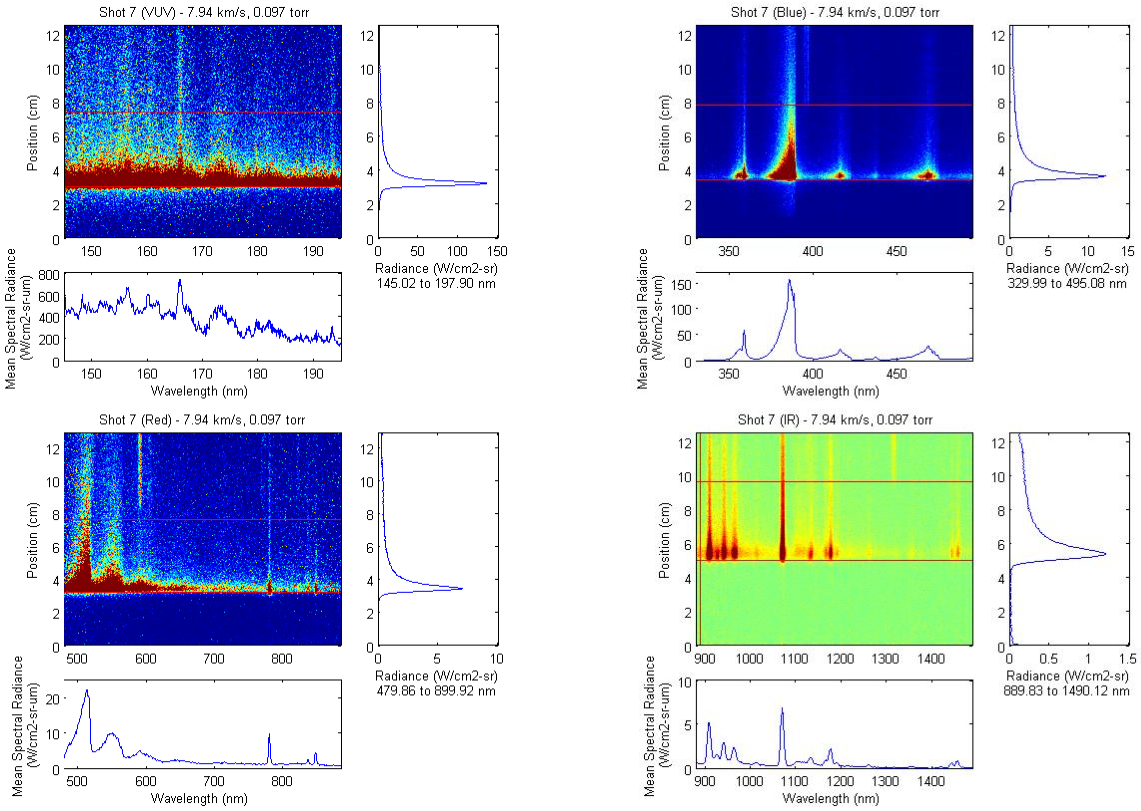

Fig. 7. Images collected on four cameras from one shot. The shock front and approximate contact front are marked by horizontal lines.

the ultraviolet (Blue) portion of the spectrum, where the appearance of Aluminum lines at 394.4 and 396.1 nm from the driver gas are readily identified. In the case of Fig. 7(b), these lines are observed at x=7.8 cm, while the shock front is at x=3.4 cm, giving a test distance of 4.4 cm. Often, the presence of tungsten and/or iron lines also accompany these Aluminum lines. In Fig. 7(b), these are very faintly observed but coincide with the x=7.8 cm contact front. In some cases, these lines will appear somewhat after the Aluminum lines. At times, faint Aluminum contamination may be observed well ahead of the actual contact front. In this case, the Aluminum may have originated from a burr on the tube wall rather than the driver. Whether or not to accept such data is subjective -- the data may be useful for comparison, but the possibility that this contamination has altered the chemistry of the shock should be taken into consideration. Fewer lines are observed in the higher wavelength visible to infrared regions of the spectrum. From Fig. 4(c) and 4(d), prominent lines are seen at 589 nm and 1314 nm and are assigned to sodium and aluminum, respectively. Sodium is not always observed in the contamination spectrum so should not be used to identify the contact front. In this case, it has appeared 5.2 cm behind the shock front so is actually behind the contact front. The Aluminum line on the IR camera is approximately 4.6 cm behind the shock front, reasonably consistent with the Blue camera image. No contamination lines are observed in the vacuum ultraviolet, but rather the radiance continually decreases due to a lower temperature and CO concentration, therefore the test length determined from the UV and/or IR spectrum must be applied to the VUV data.

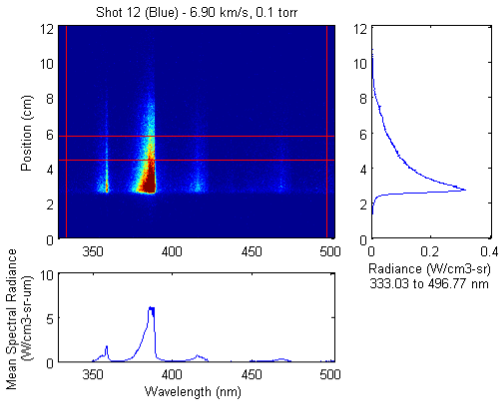

Fig. 8. Image obtained when using a Helium buffer configuration.

In some cases during Test 51, a buffer gas was employed with the intention of increasing test time. This approach was found to be successful during high speed air tests (Tests 50 and 52) by creating a buffer region between the contact front and shock front and preventing irregularities in the contact front from penetrating through the shock front. However, in the Mars test conditions, the approach proved to be less successful and made identification of the contact front more ambiguous. In this case, the contact front must be identified between the buffer gas and shocked test gas. However, since the buffer gas is composed of relatively cold helium, no strong contamination lines are observed. This is shown in Fig. 8 where the radiance simply vanishes beyond ~8 cm. In this case, the best guess of the end of the test would be where the slope suddenly changes at x=7.5 cm. In later buffer tests, argon was used instead of helium and did not show this difficulty. Buffer tests are labeled as such on the shot summary sheets.

2.2.2.2 Instrument Line Shape

Spectroscopy instrumentation has finite spectral resolution, with this attribute being referred to as the Instrument Line Shape (ILS) (and occasionally referred to as the slit function). The ILS takes into account the quality of the focusing of the light by the spectrometer in the spectrally resolved dimension and is largely determined by the width of the spectrometer slit. The slit function, however, must also be convolved with the dispersive function of the imaging media. For ICCD arrays, the dispersion due to charge bleed between adjacent pixels can have noticeable impact on the image quality. For this reason, the triangular slit function often employed in spectroscopy is a poor representation of the effective line shape. However, the lineshape is not well described by common dispersion functions such as Gaussian, Lorentzian or Voigt either.

An example of this is shown in Fig. 9, which shows the binned image of a mercury spectral line source collected with two different spectrometer systems. The resolution of these measurements is much lower than the expected width of the line source, so therefore the data may be assumed to represent the instrument line shape. While approximately 90-95% of the line intensity drops rapidly and is well fit by a Voigt, Lorentzian or Gaussian function, the remaining 5-10% decays more slowly from the line center and is not fit well by any of these functions. In some cases, it is found that this decay follows a $1/\Delta\lambda$ dependence. Two functions were found empirically to represent this line shape reasonably well, although in some cases one would fit better than the other, but not consistently so. These functions are:

$$I_1(\Delta\lambda) = \sqrt{V(\Delta\lambda)} \qquad (1)$$

$$I_2(\Delta\lambda) = \frac{G(\Delta\lambda) + 10^r L(\Delta\lambda)}{1 + 10^r} \qquad (2)$$

where V, G and L represent the Voigt, Gaussian and Lorentzian functions, respectively. Large positive values of *r* will produce a Lorentzian fit while large negative values of *r* describe a Gaussian. The quality of these two different fits is apparent from Fig. 9.

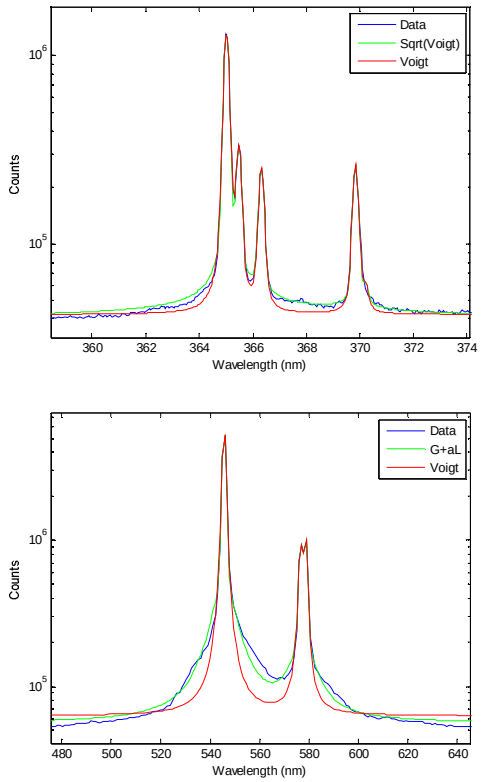

Fig. 9. Spectral images collected with Hg calibration lamps and fit with different lineshapes. (top) VUV spectrometer, (bottom) Red spectrometer.

The lineshape fits for each test series are summarized in the file Instrument Lineshapes.xls. This file gives the fit parameters for obtaining the functions I_1 and I_2 based on measurements of spectral reference sources. The file is organized into worksheets by spectrometer. Each worksheet contains two tables; the first giving a reference into the second by shot, and the second containing the fit parameters. The equation for I_1 has only two parameters, being the Gaussian and Lorentzian components of the Voigt function. The equation for I_2 has three parameters, being the Gaussian and Lorentzian components and the value of parameter *r*. In some cases, one of these components may be negligible and the corresponding fit parameters are not given. In other cases, these fit values may be given although the lineshape is not sensitive to their value. In that case, one may opt to simply use the Gaussian or Lorentzian function, as appropriate to the value of r. In the table, the Gaussian and Lorentzian components are given as half-widths with units of nm. Users will need to modify these values according to their own wavelength units and choice of half vs. full width. For NEQAIR, this amounts to multiplying these values by a factor of 20. The final item of note is that the lineshape has not been measured for every shot, so in some cases the closest available lineshape has been recommended. In these cases, this lineshape may not perfectly fit the data.

2.2.2.3 Spatial Smearing

Just as the spectral dimension of the data has finite resolution as limited by the spectrometer, resolution in spatial dimension is limited as well. This spatial resolution comes from three sources. First, the resolution of both the collection and spectrometer optics will limit how finely resolved a sharp feature in the shock tube may be. Second, the CCD itself is subject to charge smearing which will cause adjacent pixels to share intensity. Finally, the fact that the shock is moving during the exposure time will cause the shock front to blur on the camera. Each of these effects will be discussed in turn below.

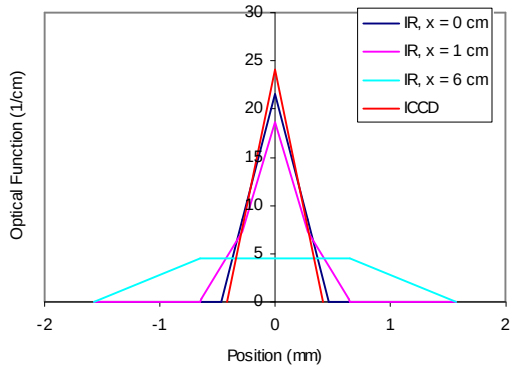

Fig. 10. Theoretical Optical Functions in EAST

The limit of optical resolution is determined by the F-number (F/#) of the system and the quality of optical alignment. The system F/# determines the nature of the optical collection volume, which may be approximated by two pyramids whose tips meet at the focal point. The internal angle of this shape is determined by the system F/#. Additionally, if the optics are telescopic, the pyramids axis may be tilted relative to its base. A telecentric optical design, as used on 3 of the 4 systems here, should result in lines of sight through the shock tube being perpendicular to the shock, or regular pyramidal volumes. From our optical design, the optical resolution is calculated as 0.8 mm for the three ICCD cameras and 3.1 mm for the IR camera. The corresponding ideal functions are shown in Fig. 10. Note that the function is triangular and independent of position for the telecentric optics, while the telescopic optics transitions from triangular

to bi-triangular to trapezoidal depending on position in the shock tube. (Note that here the position is taken as distance from the optical axis, or nominal center of the image.) While these represent the system design focus, the actual focus may be somewhat worse and may be checked by translating a calibration source over the integration path and observing the change in edge position. From this measurement, the blur was found to be between 0.3-1.4 mm for the ICCD cameras and 0.5-3.1 mm for the IR camera, in rough agreement with the calculation.

The second effect, or camera blur function, may be obtained by examining calibration data, where the edge of the calibration source is assumed to be a step transition. In such case, the derivative of the signal will give the instrument function. This function will also include the optical resolution limits related to mirror aberration and finite pixel size. An example of such a measurement is given in Fig. 11. The derivative is well fit by the functions given in eq. (1) and (2), where position x is substituted for λ. The half-widths of these measurements are generally between 0.4-4 mm, depending on the camera, however a gradual decay beyond the half-width is observed in the ICCDs.

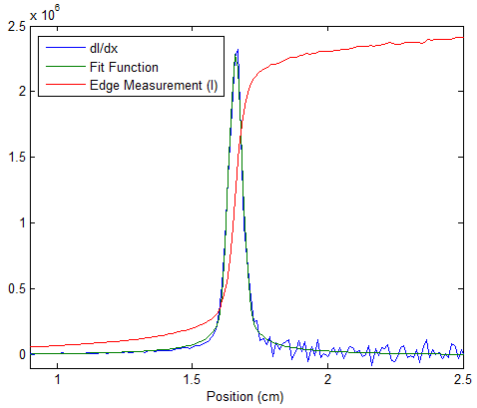

Fig. 11. Measurement of the spatial smear function

The final effect is that of the motion of the shock. At 7 km/s and an exposure time of 0.1-1.0 μs, the shock would be expected to move 0.7-7.0 mm. Since each shock has a different velocity and cameras different exposure time, each spectrometer image will have a motion blur of a distance given by vt_{exp}. At the simplest level, this may be handled as a convolution of the radiance profile with a square pulse of that distance. However, for the Red and IR cameras in particular, the pulsing function of the camera is not square with respect to time.

The exact temporal gating function may be determined by measuring the signal on the camera with a suitably fast pulsed light source. Some measurements of this nature have been made on our system. However, uncertainty in the shape of the pulse source used to make these measurements prevents us from reporting them here. Therefore, at the moment we use a square pulse for simulating the gating function, though this will require future refinement.

The net effect of the 3 sources of smearing result in a spatial profile that is broadened in comparison to the physical result. The broadening may be evaluated by convoluting predicted data with an instrument spatial function, G, which is itself a convolution of the optical, camera and motion blurring function:

$$I_{meas}(x) = \int_{-\infty}^{\infty} G(\Delta x) I_{true}(x+\Delta x)\, d\Delta x$$
$$= G(x) \otimes I_{true}(x) \qquad (4)$$
$$G(x) = f_{opt}(x) \otimes f_{cam}(x) \otimes f_{motion}(x)$$

Taking an example of the three functions discussed above, a sample convolution function is given in Fig. 12, alongside the three individual functions. The particular example is for the "Blue" camera and a shock speed of 7 km/s. In this case, it is clear that the optical function is narrower than the camera and motion functions, which have comparable widths. However, since the camera function extends over a larger distance, it tends to dominate the convolution. In the near future, these convolution functions will be compiled for the EAST data sets and made available on the website.

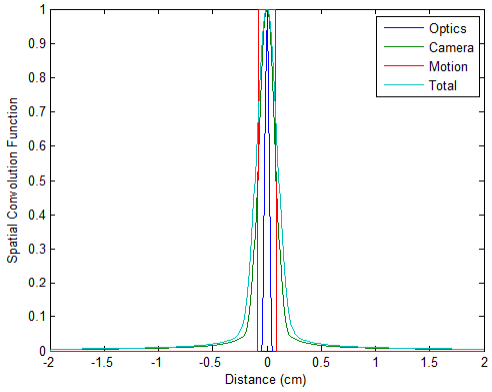

Fig. 12. Sample convolution function for the "Blue" camera at 7 km/s.

In theory, inversion of the problem to obtain the true data from the EAST data is possible when these functions are well known, however in practice the inversion carries significant noise. Regularization functions may be introduced to remove noise but may also result in blurring of real data. For this reason, the

EAST data is reported without any inversion or deconvolution.

3. CONCLUSIONS

The EAST facility at NASA Ames has been used to characterize shock-layer radiation over a wide range of conditions relevant for Mars, Venus and Earth entries. The result is a fairly sizeable database for radiance as a function of position and wavelength at prescribed conditions. The data is being made available to the research community to benchmark and improve the state of the art in radiation modelling. This paper has described general information regarding the breadth of experiments performed and how to properly interpret the data. Particular focus was given to the ESA test case conditions for Mars entries at 7-8 km/s and 0.1 and 1.0 Torr pressure. Important considerations for analysis include length of test, and finite resolution effects in both spatial and spectral dimensions. Applying proper convolution functions for these resolution limitations is important for obtaining sensible interpretation of the data.

ACKNOWLEDGEMENTS

The author would like to acknowledge the work of the EAST facility crew, including Mark McGlaughlin, Ramon Martinez and James Joyce in obtaining the EAST data. Useful discussions with the Ames Radiation group, including Drs. Dinesh Prabhu, Michael Winter, Aaron Brandis, Deepak Bose and David Bogdanoff, are also acknowledged. The Fundamental Aeronautics Hypersonics program, AAP discipline is acknowledged for financial support. The author is support by NASA contract NAS2-99092 to ERC Corporation.